

Climatic control on the location of the Southern Andes volcanic arc

Veleda Paiva Muller (✉ v.paivamuller@campus.unimib.it)

University of Milano-Bicocca <https://orcid.org/0000-0001-6808-3509>

Pietro Sternai

University of Milano-Bicocca

Christian Sue

Université Grenoble Alpes

Article

Keywords: Southern Andes Volcanic Zone, volcanic arc, climatic control

Posted Date: June 4th, 2021

DOI: <https://doi.org/10.21203/rs.3.rs-567948/v1>

License: © ⓘ This work is licensed under a Creative Commons Attribution 4.0 International License.

[Read Full License](#)

Climatic control on the location of the Southern Andes volcanic arc

Veleda Astarte Paiva Muller*¹, Pietro Sternai¹, Christian Sue²

*Corresponding Author

¹Dipartimento di Scienze dell'Ambiente e della Terra, Università degli Studi di Milano-Bicocca, Piazza della Scienza, 4, Milan, Italy. v.paivamuller@campus.unimib.it; pietro.sternai@unimib.it

²CNRS, IRD, IFSTTAR, ISTERre, University Grenoble Alpes, University Savoie Mont Blanc, 38000 Grenoble, France. christian.sue@univ-grenoble-alpes.fr; also at UMR6249, Université de Bourgogne Franche-Comté, UFC, Besançon, France

Volcanic arcs at convergent plate margins are primary surface expressions of plate tectonics. Although climate affects many of the manifestations of plate tectonics via erosion, the upwelling of magmas and location of volcanic arcs are considered insensitive to climate. In the Southern Andes, subduction of the Nazca oceanic plate below the South American continent generates the Southern Andes Volcanic zone. Orographic interactions with Pacific westerlies lead to high precipitation and erosion on the western slopes of the belt between 42-46°S. At these latitudes, the topographic water divide and the volcanic arc are respectively farther and closer to the subduction trench than at lower latitudes, despite a constant subduction dip angle along strike. Here, we use thermomechanical numerical modeling to investigate how magma upwelling is affected by topographic changes due to orography. We show that a leeward topographic shift may entail a windward asymmetry of crustal structures accommodating the magma upwelling, consistent with the observed trench-ward migration of the Southern Andes Volcanic Zone. A climatic control on the location of volcanic arcs via orography and erosion is thus revealed.

Southern Andes volcanic arc and climate

Dehydration of a subducting oceanic plate commonly occurs at ~100 km depth and leads to partial melting of mantle rocks^{1,2}. Upwelling buoyant magmas then feed the volcanic arc on the upper continental plate¹⁻⁵. The slab dip angle, thus, exerts a primary control on the distance between the volcanic arc and the subduction trench^{2,6}, while crustal and lithospheric structures affect the magma ascent toward the surface³⁻⁵. The topography generated by compressional strain and magma upwelling during ocean-continent subduction is subject to climate-driven erosion⁷⁻¹¹. The redistribution of the surface masses by erosion, in turn, affects the lithospheric deformation, partial rock melting, and magma transfer, thereby influencing the structural and magmatic evolution of a compressional orogen⁷⁻¹³. If the topography acts as an orographic barrier, in particular, enhanced precipitation and erosion on the upwind side of the orogen force a leeward migration of the topographic range⁹. While the role of orography and associated erosion gradients on the structure and topography of an orogen was addressed before⁷⁻¹⁰, its forcing on the location of a volcanic arc has been overlooked.

In the Southern Andes between ~34-46°S, subduction of the Nazca oceanic plate beneath South America bounded to the south by the northward migrating Chile Triple Junction (CTJ) generates the Southern Andes Volcanic Zone (SVZ) and an orogenic wedge with mean elevation between 1-3 km above sea level¹⁴⁻²⁰ (Fig. 1a). Throughout the Plio-Quaternary, steady oblique subduction along strike occurs at a rate of ~7 cm/yr (Refs. 21-23) with slab dip angle of ~25° (Refs. 24-26). Three latitudinal zones account for statistically significant changes in the relative distances between the subduction trench, the topographic water divide, and Quaternary volcanoes (Fig. 1, Supplementary Table 1, Methods). The average distance between each volcano and the

subduction trench decreases from ~300 km north of 42°S (zones 1 and 2), where volcanoes are located above the 100 and 120 km slab isodepths, to ~260 km south of ~42°S (zone 3), where volcanoes are located above the 80 and 100 km slab isodepths (Fig. 1a,b). This ~40 km trenchward migration of the volcanic arc between zones 1-2 and zone 3 cannot be explained by a southward increase in the slab dip angle^{24–26}. Instead, south of ~40°S the amount of precipitation increases on the western slopes due to orographic interactions with westerly winds²⁷. The increase in erosion rates on the upwind side of the range^{28,29} leads to a ~70 km eastward migration of the topographic water divide (Fig. 1c) and contributes to a ~1000 m decrease in the mean altitude^{15,18,20} of the orogenic wedge from zone 1 to 3. Volcanoes are found west and east of the topographic water divide north of ~40°S, but they are systematically west of the water divide south of ~40°S (Fig. 1a,d).

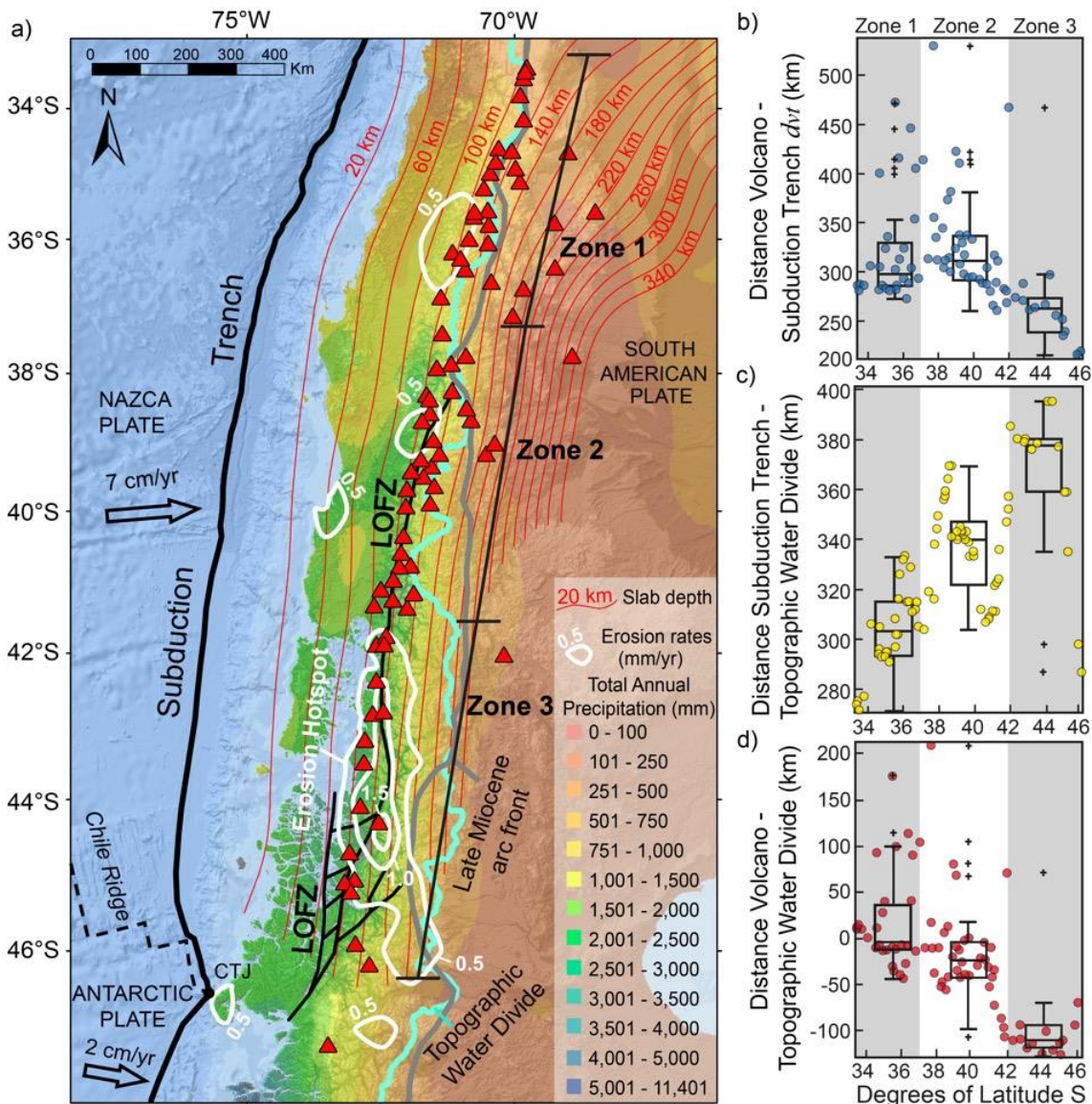


Fig. 1. Synoptic view of the study region and data analyses. **a**, Map of total annual precipitation³⁰ in the Southern Andes with Quaternary volcanoes (red triangles³¹) divided in three latitudinal zones for analysis (Methods). Quaternary erosion rates²⁹. Convergence plates velocities²¹. Depth of the top of the Nazca slab^{25,26}. Late Miocene arc front adapted from¹⁹. **b-d**, Scatter and box plots of the relative distances between the volcanoes, the subduction trench and the topographic water divide (Supplementary Table 1). Negative values indicate volcanoes to the west of the water divide. Whiskers (w) extend to the most extreme data points (without considering outliers, plotted with '+' (Supplementary Table 1), and correspond to ~2.7 σ and 99.3% coverage of the data. Outliers, defined as values greater than $q_3 + w(q_3 - q_1)$ or smaller than $q_1 - w(q_3 - q_1)$, where q_1 and q_3 are the first and third quartiles respectively, correspond to within-plate volcanoes¹⁹ located more than 400 km east of the subduction trench.

Numerical analysis

We use a lithosphere-asthenosphere thermomechanical visco-elasto-plastic numerical geodynamic model (see Methods) to test the hypothesis of an upwind (i.e., trench-ward) migration

of the SVZ forced by orography. A mantle-melting zone (MMZ) with 20 km diameter is imposed in the center of the model domain. The upward transfer and emplacement of magma into the crust occurs through a 3 km wide magmatic channel, which allows for a simplified representation of magmatic percolation by hydrofractures³⁻⁵, diffusion³², porous flow³³, and reactive flow³⁴ through the rheologically stronger mantle lithosphere³⁵ (Supplementary Table 2). The parametric study (Supplementary Table 3) focuses on (1) the crustal thickness (Ch, equal to 35 and 45 km^{14,17,18,25}), (2) the initial depth of the magmatic channel upper tip³⁵ (Dmc, equal to 15, 20, and 25 km) and, (3) the lithospheric thickness (Lh, equal to 90 and 100 km^{14,17,25}). In order to investigate how the topographic load affects the magma upwelling path, all model configurations were tested with an initial central and lateral (i.e., shifted rightward with respect to the MMZ) topographic wedge on the model free surface (Fig. 2 and Supplementary Figs. 1-4). This choice implies that, for each model configuration, simulations with central and lateral topography show the paths of magma upwelling prior to and after the landscape has adjusted to the orographic gradient, respectively (the transient state is beyond our purpose). In order to isolate the effects of topographic changes on magma upwelling, we did not impose tectonic convergence in the models, which simply evolve by upwelling of buoyant magma into the crust until depletion of the MMZ in about 0.2 Myr (Fig. 2 and Supplementary Figs. 1-4).

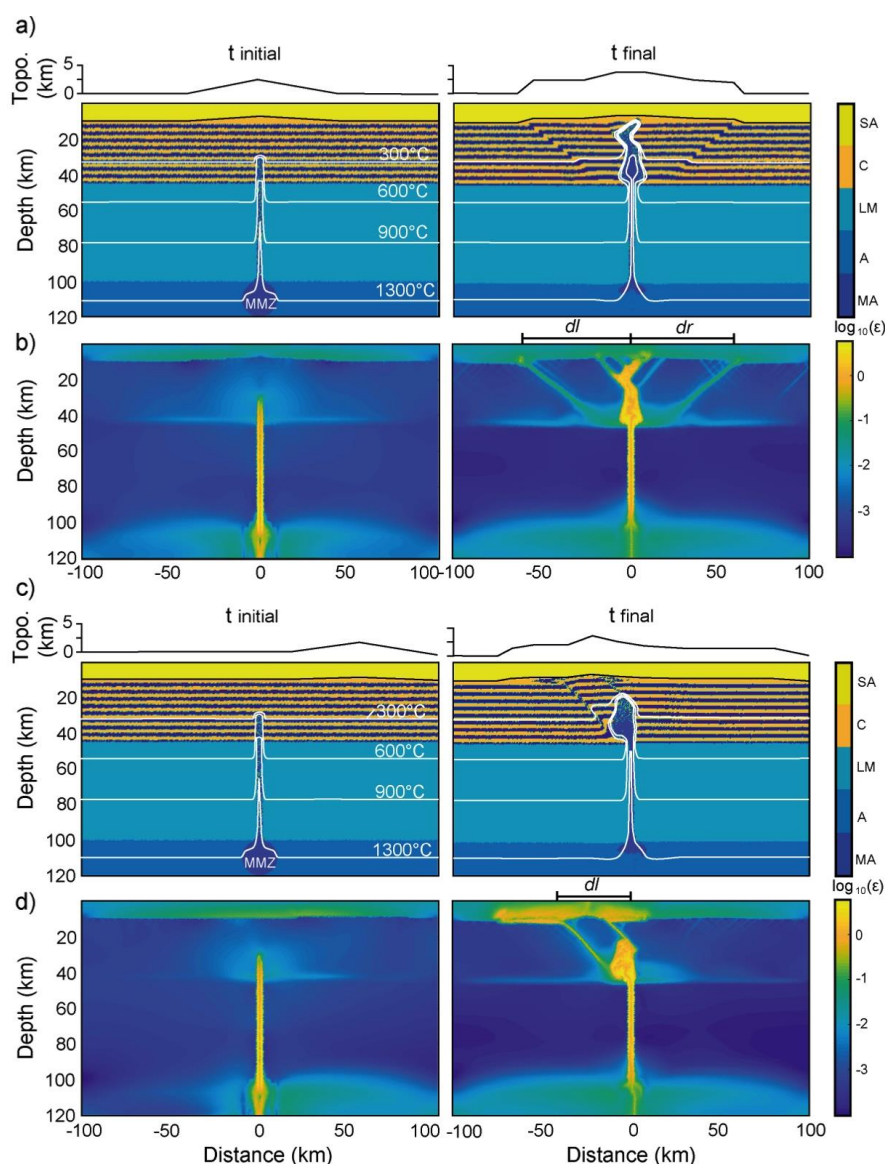


Fig. 2. Initial and final steps of selected numerical simulations (Ch = 35, Lh = 100, Dmc = 20 km). Color layering in the crust is to show deformation. The topographic profiles shown above the simulation have 3x of vertical exaggeration. Lithological and thermal distribution (a) and cumulative bulk strain (b) of the numerical model with central topographic wedge above the MMZ. Note the symmetric final system of brittle-ductile structures accommodating the rise of magma to near the surface. Lithological and thermal distribution (c) and cumulative bulk strain (d) of the numerical model with topographic wedge to the right of the MMZ. The final system of brittle-ductile structures is asymmetric (leftward), leading to distal magma upwelling from the initial topographic wedge. *dr* and *dl* are defined in the text. SA – sticky air; C – crust; LM – lithospheric mantle; A – asthenosphere; MA – molten asthenosphere.

The emplacement of magma into the crust is accommodated by strain structures, which interest the brittle upper crust and the ductile lower crust. Simulations that account for a central

topographic wedge show the formation of symmetric crustal magma reservoir and strain structures with respect to the MMZ, feeding volcanoes on both sides of the topographic wedge (Fig. 2a,b and 3). Simulations that account for a lateral topographic wedge develop highly asymmetric crustal magma reservoirs and strain structures, feeding volcanoes on the opposite side of the topographic wedge (Figs. 2c,d and 3).

The degree of asymmetry of the accumulated strain at the end of the simulations is defined as $\delta d = |dr| - |dl|$, where dr and dl are the maximum horizontal distance between the center of the model domain and the surface fault tips to the right (positive values) and left (negative values) respectively (Fig. 2b,d; Supplementary Figures 1-4 and Supplementary Table 3). When the topography is shifted laterally, a thin crust ($Ch = 35$ km) enhances the asymmetry of strain and magma upwelling (Figs. 2, 3, and Supplementary Figs. 1 and 2). This general trend is largely independent on Dmc and Lh . When the crust is thick ($Ch = 45$ km) and Dmc is high (25 km), the viscous strain in the lower crust accommodates almost entirely the emplacement of magma, inhibiting the formation of upper crustal brittle structures and the rise of magma to the near surface (Fig. 3 and Supplementary Figs. 3,4). Regardless of the crustal and lithospheric thickness, when Dmc is low (15 km), the magma rises easily to the surface through brittle structures near the center of the model, resulting on relatively small values of δd (Fig. 3 and Supplementary Figs. 1-4). When Dmc is intermediate (20 km), brittle-ductile structures cross through the crust reaching the surface at further distance from the center of the model (Figs. 2, 3, and Supplementary Figs. 1,3,4). This results into a highly asymmetric magma upwelling system when topography is shifted laterally (*i.e.* high, negative δd value, Figs. 2d and 3). The reference model (Fig. 2) shows $\delta d = \sim -40$ km, consistent with the observed trench-ward shift of the volcanic arc in zone 3 compared to zones 1 and 2 (Fig. 1a,b).

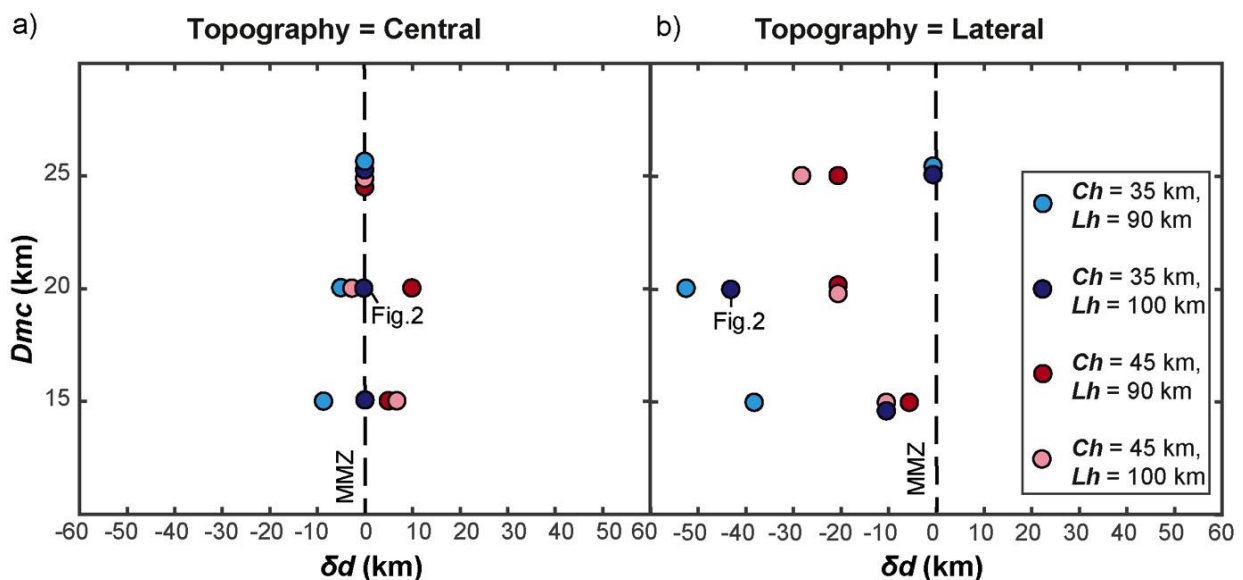


Fig. 3. Results of the parametric study. Initial depth of the magmatic channel upper tip (Dmc) vs. degree of asymmetry in cumulative strain (δd , see text), with central (a) and lateral topography (b). Negative values show asymmetry to the left of the MMZ. Values for Ch and Lh are shown in the legend, cold and hot colors show simulations with thin and thick crust, respectively. See results of simulations on Fig. 2, Supplementary Figs. 1-4 and Table 3.

Tectonics, orography and volcanic arcs

The topography of an orogen commonly adjusts to lateral erosional gradients over timescales between 0.01-0.1 Ma (Ref. 36), which are significantly shorter than the Pliocene to

present interval, during which orography and the onset of glaciation conditioned the orogen growth^{28,29,37} in absence of major tectonic changes^{22,23,38,39}. We can thus interpret our results in the light of the multi-Ma timescale orogenic and volcanic arc evolution.

The break-up of the Farallon Plate into the Nazca and Cocos oceanic plates^{22,23} enhanced compressional stresses and mountain building across the Southern Andes in the Miocene^{20,37-41}. South of $\sim 40^\circ\text{S}$, strain localization along the transpressive Liquiñe-Ofqui Fault Zone (LOFZ) since at least the Pliocene^{15,28,42} is related to the oblique convergence of the Nazca Plate and/or the CTJ approaching its current position^{15,16,28,41-43}. Trench-ward migration of the Late Miocene volcanic arc to its current position is ascribed to the activation of the LOFZ which accommodates magma upwelling^{15,38,40} (Figs. 1a and 4b) and/or a slab steepening event^{17,19,40}. Our models show that a thinner crust such as that between $\sim 42-46^\circ\text{S}$ is more prone to localized strain structures that may accommodate the magma upwelling and migration of the volcanic arc (Figs. 2-3), as previously suggested¹⁸. Results, however, further show that also an orographic shift of the topographic load during magma upwelling can foster the formation of localized strain structures toward regions of enhanced erosion and reduced topographic load. If these structures serve as a main path for the magma ascent as suggested for the LOFZ^{15-18,28,40-43}, then a leeward orographic shift of the topography can facilitate an upwind migration of the volcanic arc (Fig. 4). Our results explain observations (Fig. 1) without requiring a contribution by northward migration of the CTJ nor a change in slab dip angle, although we do not dismiss these factors. We thus propose that, following the Miocene fragmentation of the Farallon slab and associated topographic growth^{20,22,23,37-41}, a Plio-Quaternary trench-ward migration of the strain and the volcanic arc south of $\sim 40^\circ\text{S}$ is fostered jointly by the established orographic erosion gradient, the approach of the CTJ to its present position^{28,41,43} and possibly a slab steepening event^{19,40}. In this view, heat advection from the approaching CTJ^{28,39} was enhanced by higher orographic erosion on the windward side of the orogen, weakening the crust and fostering the activation the LOFZ and westward volcanic arc migration.

The climatic control on magmatism, thus, occurs not only through a forcing from ice building-melting^{12,13}, erosion^{11,44} and/or sea level changes⁴⁵ on the magma production, but also through an orographic forcing on the magma upwelling path, affecting the location of volcanic arcs. We expect this recognition to be broadly applicable to other volcanic arcs worldwide and particularly relevant for volcanic arc ore deposits, the exploitation of which is primarily conditioned by the regional topography itself. Because volcanic arcs provide a substantial contribution to the evolution of climate across timescales, this recognition provides an additional evidence of the tight coupling between climate and plate tectonics^{46,47}.

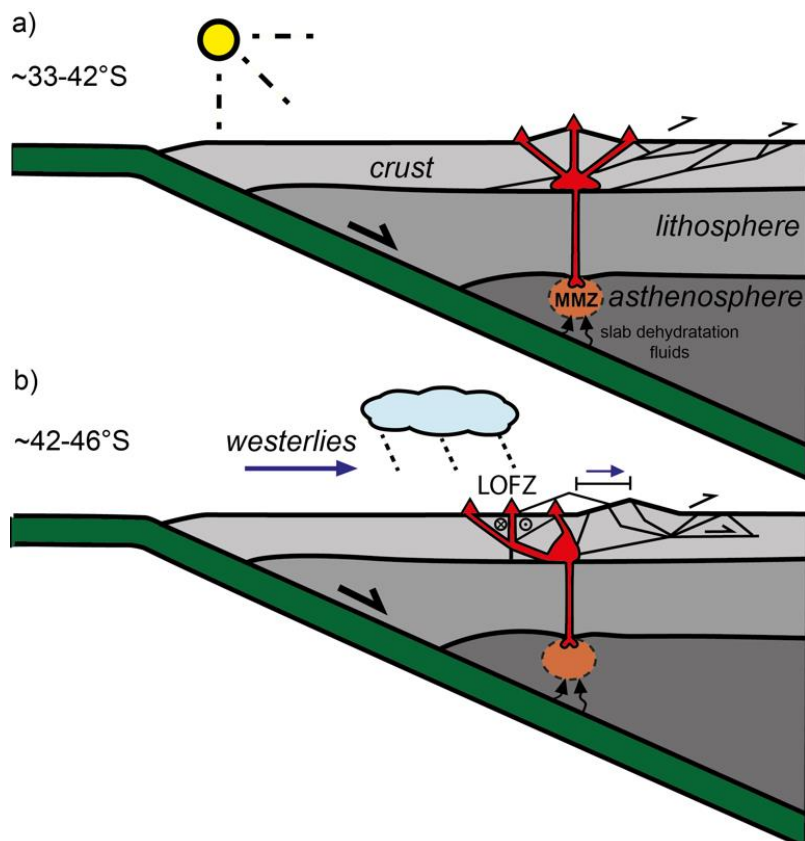


Fig. 4. Schematic model of the orographic forcing on the location of the SVZ. **a**, Analogy for zones 1-2 (~33-42°S), with relatively symmetric climate, erosion rates, and volcanoes position with respect to the orogenic wedge, structures are simplified from²⁰. **b**, Analogy for zone 3 (~42-46°S), with asymmetric climate, erosion rates and volcanoes position due to westerly storm-tracks, driving leeward migration of the orogenic wedge and upwind migration of the deformation, structures are simplified from⁴⁰ and the LOFZ is represented as a preferential channel for magma upwelling.

Acknowledgements

This work part of the project MIUR – Dipartimenti di Eccellenza 2018–2022, Department of Earth and Environmental Sciences, University of Milano-Bicocca. PS was supported by the Italian MIUR (Rita Levi Montalcini grant, DM 694–26/2017). CS was supported by the University of Grenoble-Alpes.

Online Content

Methods, Additional References, and Supplementary Tables and Figures are available for this paper.

Authors Contributions

VAPM contributed to the development of the initial scientific question, performed the study and wrote the manuscript. PS conceived the initial scientific question, helped with the data interpretation and numerical investigation, and contributed the manuscript writing. CS contributed to the development of the initial scientific questions, helped with the interpretation of the geological data and numerical models, and contributed to manuscript writing.

Competing interest declaration

The authors declare no competing interests.

Corresponding Author line

Correspondence and request for materials should be addressed to VAPM.

References

1. Peacock, S. M. Processes Subduction Zones. *Science* (80-.). **329**, 329–337 (1990).
2. England, P. C. & Katz, R. F. Melting above the anhydrous solidus controls the location of volcanic arcs. *Nature* **467**, 700–703 (2010).
3. Nakamura, K. Volcanoes as possible indicators of tectonic stress orientation - principle and proposal. *J. Volcanol. Geotherm. Res.* **2**, 1–16 (1977).
4. Clemens, J. D. & Mawer, C. K. Granitic magma transport by fracture propagation. *Tectonophysics* **204**, 339–360 (1992).
5. Petford, N., Cruden, A. R., McCaffrey, K. J. W. & Vigneresse, J. L. Granite magma formation, transport and emplacement in the Earth's crust. *Nature* **408**, 669–673 (2000).
6. Coney, P. J. & Reynolds, S. J. Cordilleran Benioff Zones. *Nature* **270**, 403–406 (1977).
7. Dahlen, F. A., Suppe, J. & Clark, S. P. Mechanics, growth and erosion of mountain belts. in *Processes in Continental Lithospheric Deformation* (eds. Clark, S. P., Burchfiel, C. B. & Suppe, J.) 161–178 (Geological Society of America, 1988).
8. Molnar P. & England P. Late Cenozoic Uplift of Mountain Ranges and Global Climate Change: Chiken or Egg? *Nature* **346**, 29–34 (1990).
9. Willett, S. D. Orogeny and orography: The effects of erosion on the structure of mountain belts. *J. Geophys. Res. Solid Earth* **104**, 28957–28981 (1999).
10. Whipple, K. X. The influence of climate on the tectonic evolution of mountain belts. *Nat. Geosci.* **2**, 97–104 (2009).
11. Sternai, P. Surface processes forcing on extensional rock melting. *Sci. Rep.* **10**, 1–14 (2020).
12. Sigvaldason, G. E., Annertz, K. & Nilsson, M. Effect of glacier loading/deloading on volcanism: postglacial volcanic production rate of the Dyngjufjoll area, central Iceland. *Bull. Volcanol.* **54**, 393–404 (1992).
13. Jull, M. & McKenzie, D. The effect of deglaciation on mantle melting beneath Iceland. *Eff. deglaciation mantle melting beneath Icel.* **101 B10**, 21815–21828 (1996).
14. Hildreth, W. & Moorbath, S. Crustal contributions to arc magmatism in the Andes of Central Chile. *Contrib. to Mineral. Petrol.* **98**, 455–489 (1988).
15. Hervé, F. The Southern Andes Between 39° and 44°S Latitude: The Geological Signature of a Transpressive Tectonic Regime Related to a Magmatic Arc. in *Tectonics of the Southern Central Andes* (eds. Reutter, K.-J., Scheuber, E. & Wigger, P. J.) 243–248 (Springer, 1994).
16. López Escobar, Á., Cembrano, J. & Moreno, H. Geochemistry and tectonics of the Chilean Southern Andes basaltic Quaternary volcanism (37–46°S). *Andean Geol.* **22**, 219–234 (1995).
17. Stern, C. R. Active Andean Volcanism: its geologic and tectonic setting. *Rev. Geol. Chile* **31**, 161–206 (2004).
18. Cembrano, J. & Lara, L. The link between volcanism and tectonics in the southern volcanic zone of the Chilean Andes: A review. *Tectonophysics* **471**, 96–113 (2009).
19. Folguera, A. & Ramos, V. A. Repeated eastward shifts of arc magmatism in the Southern Andes: A revision to the long-term pattern of Andean uplift and magmatism. *J. South Am. Earth Sci.* **32**, 531–546 (2011).
20. Giambiagi, L., Mescua, J., Bechis, F., Tassara, A. & Hoke, G. Thrust belts of the southern Central Andes: Along-strike variations in shortening, topography, crustal geometry, and

- denudation. *Bull. Geol. Soc. Am.* **124**, 1339–1351 (2012).
21. DeMets, C., Gordon, R. G. & Argus, D. F. Geologically current plate motions. *Geophys. J. Int.* **181**, 1–80 (2010).
 22. Lonsdale, P. Creation of the Cocos and Nazca plates by fission of the Farallon plate. *Tectonophysics* **404**, 237–264 (2005).
 23. Seton, M. *et al.* Global continental and ocean basin reconstructions since 200Ma. *Earth-Science Rev.* **113**, 212–270 (2012).
 24. Barazangi, M. & Isacks, B. L. Spatial distribution of earthquakes and subduction of the Nazca plate beneath South America: Comment. *Geology* **4**, 686–692 (1976).
 25. Tassara, A. & Echaurren, A. Anatomy of the Andean subduction zone: Three-dimensional density model upgraded and compared against global-scale models. *Geophys. J. Int.* **189**, 161–168 (2012).
 26. Hayes, G. P. *et al.* Slab2, a comprehensive subduction zone geometry model. *Science* (80-). **362**, 58–61 (2018).
 27. Garreaud, R., Lopez, P., Minvielle, M. & Rojas, M. Large-scale control on the Patagonian climate. *J. Clim.* **26**, 215–230 (2013).
 28. Thomson, S. N. Late Cenozoic geomorphic and tectonic evolution of the Patagonian Andes between latitudes 42°S and 46°S: An appraisal based on fission-track results from the transpressional intra-arc Liquiñe-Ofqui fault zone. *Bull. Geol. Soc. Am.* **114**, 1159–1173 (2002).
 29. Herman, F. & Brandon, M. Mid-latitude glacial erosion hotspot related to equatorial shifts in southern Westerlies. *Geology* **43**, 987–990 (2015).
 30. Hijmans, R. J., Cameron, S. E., Parra, J. L., Jones, P. G. & Jarvis, A. Very high resolution interpolated climate surfaces for global land areas. *Int. J. Climatol.* **25**, 1965–1978 (2005).
 31. Venzke, E. Global Volcanism Program. *Volcanoes of the World* (2013) doi:<https://doi.org/10.5479/si.GVP.VOTW4-2013>.
 32. Scambelluri, M. & Philippot, P. Deep fluids in subduction zones. *Lithos* **55**, 213–227 (2001).
 33. Connolly, J. A. D. & Podladchikov, Y. Y. Compaction-driven fluid flow in viscoelastic rock. *Geodin. Acta* **11**, 55–84 (1998).
 34. Spiegelman, M. & Kelemen, P. B. Extreme chemical variability as a consequence of channelized melt transport. *Geochemistry, Geophys. Geosystems* **4**, (2003).
 35. Gerya, T. V. *Introduction to Geodynamic Numerical Modeling*. (Cambridge University Press, 2019).
 36. Whipple, K. X. & Tucker, G. E. Dynamics of the stream-power river incision model: Implications for the height limits of mountain ranges, landscape response timescales, and research need. *J. Geophys. Res.* **104**, 661–674 (1999).
 37. Stalder, N. F. *et al.* The relationships between tectonics, climate and exhumation in the Central Andes (18–36°S): Evidence from low-temperature thermochronology. *Earth-Science Rev.* **210**, (2020).
 38. Echaurren, A. *et al.* Tectonic evolution of the North Patagonian Andes (41°–44° S) through recognition of syntectonic strata. *Tectonophysics* **677–678**, 99–114 (2016).
 39. Folguera, A. *et al.* Constraints on the Neogene growth of the central Patagonian Andes at the latitude of the Chile triple junction (45–47°S) using U/Pb geochronology in synorogenic strata. *Tectonophysics* **744**, 134–154 (2018).
 40. Orts, D. L. *et al.* Tectonic development of the North Patagonian Andes and their related

Miocene foreland basin (41°30'-43°S). *Tectonics* **31**, (2012).

41. Lagabriele, Y. *et al.* Neogene to Quaternary tectonic evolution of the Patagonian Andes at the latitude of the Chile Triple Junction. *Tectonophysics* **385**, 211–241 (2004).
42. Cembrano, J., Schermer, E., Lavenu, A. & Sanhueza, A. Contrasting nature of deformation along an intra-arc shear zone, the Liquine-Ofqui fault zone, southern Chilean Andes. *Tectonophysics* **319**, 129–149 (2000).
43. De Pascale, G. P. *et al.* Liquiñe-Ofqui's fast slipping intra;volcanic arc crustal faulting above the subducted Chile Ridge. *Sci. Rep.* 1–12 (2021).
44. Sternai, P., Caricchi, L., Castelltort, S. & Champagnac, J. D. Deglaciation and glacial erosion: A joint control on magma productivity by continental unloading. *Geophys. Res. Lett.* **43**, 1632–1641 (2016).
45. Crowley, J. W., Katz, R. F., Huybers, P., Langmuir, C. H. & Park, S. Production of Oceanic Crust. *Science (80-.)*. **347**, 1237–1240 (2015).
46. Sternai, P. *et al.* Magmatic Forcing of Cenozoic Climate? *J. Geophys. Res. Solid Earth* **125**, 1–22 (2020).
47. McKenzie, N. R. *et al.* Continental arc volcanism as the principal driver of icehouse-greenhouse variability. *Science (80-.)*. **352**, 444–447 (2016).

Methods

Measurements of volcano-trench-water divide distances and zonal analysis

The relative distances between the volcanoes, the subduction trench, and the topographic water divide were measured based on volcanoes coordinates provided by Ref. 31. The location of the subduction trench and the topographic water divide was traced using Google Earth at a scale ~1:4,000,000. Measurements (Supplementary Table 1) account for the closer point along the trench and the closer point along the water divide to each volcano. The subdivision of the SVZ in zones 1, 2 and 3 is based on the petrochemical and structural arrangement of the arc^{16–19} and help us to highlight meaningful correlations between measured distances.

Thermomechanical model

The numerical model is based on conservative finite-differences with marker-in-cell technique and incorporates temperature-dependent rheologies for solid and partially molten rocks^{35,48}. The model accounts for a (1) mechanical, (2) visco-elasto-plastic rheological, (3) thermal, and (4) partial rock melting component. A short description of the models' components is provided hereafter. Additional details and full description of the numerical techniques are provided elsewhere^{11,35,49}.

Mechanical Component

The continuity equation (1)

$$(1) \frac{\partial \rho}{\partial t} + \nabla(\rho \vec{v}) = 0,$$

where ρ is the local density, t is time, \vec{v} is the velocity vector, and ∇ is the divergence operator, allows for the conservation of mass during the displacement of a geological continuum.

The momentum equation (2)

$$(2) \frac{\partial \sigma_{ij}}{\partial x_i} + \rho g_i = \rho \left(\frac{\partial v_i}{\partial t} + v_j \frac{\partial v_i}{\partial x_j} \right),$$

where σ_{ij} is the stress tensor, x_i and x_j are spatial coordinates, and g_i is the i -th component of the gravity vector, describes the changes in velocity of an object in the gravity field due to internal and external forces.

Rheological Component

Ductile deformation is thermally activated and occurs by viscous flow. Diffusion and dislocation creep are computed based on material viscosity shear viscosity^{35,49}, $\eta_{ductile}$ (equation 3), defined as:

$$(3) \frac{1}{\eta_{ductile}} = \frac{1}{\eta_{diff}} + \frac{1}{\eta_{disl}}, \text{ with}$$

$$(3.1) \eta_{diff} = \frac{\eta_0}{2\sigma_{cr}^{n-1}} \exp\left(\frac{E_a + PV_a}{RT}\right), \text{ and}$$

$$(3.2) \eta_{disl} = \frac{\eta_0^{\frac{1}{n}}}{2} \exp\left(\frac{E_a + PV_a}{nRT}\right) \epsilon_{II}^{\frac{1}{n}-1},$$

where, η_{diff} (equation 3.1) and η_{disl} (equation 3.2) are the shear viscosity for diffusion and

dislocation creep, respectively, η_0 is the material static viscosity, σ_{cr} is the diffusion-dislocation transition critical stress, n is the stress exponent, E_a is the activation energy, V_a is the activation volume, P is pressure, R is the gas constant, T is the temperature, and ε'_{II} is the second invariant of the strain rate tensor. Then, the viscous deviatoric strain rate tensor, $\dot{\varepsilon}'_{ij (viscous)}$ (equation 4), is computed as:

$$(4) \dot{\varepsilon}'_{ij (viscous)} = \frac{1}{2\eta_{ductile}} \sigma'_{ij} + \delta_{ij} \eta_{bulk} \dot{\varepsilon}_{kk} = \frac{1}{2\eta_{diff}} \sigma'_{ij} + \frac{1}{2\eta_{dist}} \sigma'_{ij} + \delta_{ij} \eta_{bulk} \dot{\varepsilon}_{kk},$$

where, σ'_{ij} is the deviatoric stress tensor, δ_{ij} is the Kronecker delta, $\dot{\varepsilon}_{kk}$ is the volumetric strain rate (e.g., related to phase transformations), η_{bulk} is the bulk viscosity.

Elastic deformation is reversible and assumes proportionality of stress and strain. The elastic deviatoric strain rate tensor, $\dot{\varepsilon}'_{ij (elastic)}$ (equation 5), is computed as:

$$(5) \dot{\varepsilon}'_{ij (elastic)} = \frac{1}{2\mu} \frac{\check{D}\sigma'_{ij}}{Dt},$$

where, μ is the shear modulus, and $\frac{\check{D}\sigma'_{ij}}{Dt}$ is the objective co-rotational time derivative of the deviatoric stress tensor.

Plastic (or brittle) localised deformation occurs at low temperature in the upper part of the lithosphere, after reaching the absolute shear stress limit, σ_{yield} (equation 6), is defined as:

$$(6) \sigma_{yield} = C + \sin(\varphi)P,$$

where, C is cohesion, φ is the effective internal friction angle. The plastic strain rate tensor, $\dot{\varepsilon}'_{ij (plastic)}$ (equation 7), is then computed as:

$$(7) \dot{\varepsilon}'_{ij (plastic)} = 0 \text{ for } \sigma_{II} < \sigma_{yield}, \dot{\varepsilon}'_{ij (plastic)} = \mathcal{X} \frac{\partial \sigma'_{ij}}{2\sigma_{II}} \text{ for } \sigma_{II} \geq \sigma_{yield},$$

where \mathcal{X} is the plastic multiplier which satisfies the plastic yielding condition $\sigma_{II} = \sigma_{yield}$.

At the lithospheric scale, all deformation mechanisms occur jointly and the overall visco-elasto-plastic rock strain rate tensor, $\dot{\varepsilon}'_{ij (bulk)}$ (equation 8), is defined as:

$$(8) \dot{\varepsilon}'_{ij (bulk)} = \dot{\varepsilon}'_{ij (viscous)} + \dot{\varepsilon}'_{ij (elastic)} + \dot{\varepsilon}'_{ij (plastic)}$$

Thermal Component

Heat conservation during advective and conductive heat transfer in the continuum is computed by the energy equation (9):

$$(9) \rho C_p \frac{DT}{Dt} - \text{div}(c\nabla T) + v\nabla T = H_r + H_s + H_a + H_l,$$

where C_p is specific heat capacity at a constant P , c is the thermal conductivity, $H_r + H_s + H_a + H_l$ are the volumetric heat productions by radiogenic, shear, adiabatic and latent heat, respectively. $H_a \propto \frac{DP}{Dt}$, $H_s = \sigma'_{ij} \dot{\varepsilon}'_{ij (viscous)}$, and H_r and H_l are defined in Supplementary Table 2.

Partial Melting Component

Partial melting occurs between the wet solidus, T_s , and dry liquidus, T_l , of the considered lithologies^{50–52} (Supplementary Table 2). ξ is the volumetric fraction of melt (equations 10.1 –

10.3) that increases linearly with T at a constant P (Ref. 53), so that,

$$(10.1) \xi = 0 \text{ at } T \leq T_s$$

$$(10.2) \xi = 1 \text{ at } T \geq T_l$$

$$\text{and (10.3) } \xi = \frac{(T-T_s)}{(T_l-T_s)} \text{ at } T_s < T < T_l$$

The effective density, ρ_{eff} (equation 11), of partially molten rocks is then computed by^{11,35}:

$$(11) \rho_{eff} = \rho_s (1 - \xi + \xi \frac{\rho_l^0}{\rho_s^0}),$$

where ρ_l^0 and ρ_s^0 are the standard densities of solid and molten rocks, respectively. The solid rock density, ρ_s (equation 12), is calculated as³⁵:

$$(12) \rho_s = \rho_o [1 + \beta(P - P_o)] \times [1 - \alpha(T - T_o)],$$

where β is compressibility, α is thermal expansion and ρ_o , P_o , and T_o are density, pressure and temperature of rocks at surface conditions.

Reference Model Setup

The initial setup measures 200 × 120 km in the x and y dimensions (Fig. 2), resolved by 201 × 61 grid points respectively, distributed on an irregular Eulerian grid that accounts for a maximum resolution of 1 km along the x and y directions in the upper-central part of the model domain. 400 × 400 Lagrangian markers are randomly distributed along the x and y dimensions and used for advecting the material properties^{11,35,49}. The material properties carried by Lagrangian markers are then interpolated onto the Eulerian grid via a 4th order Runge-Kutta interpolation scheme^{35,49}. An internal free surface is simulated through a 10 km thick layer of sticky air⁴⁹. The velocity boundary conditions are free slip at all boundaries (x = 0 and x = 200 km; y = 0 and y = 120 km). The initial temperature gradient is piece-wise linear resulting from an adiabatic temperature gradient of 0.5 °C/km in the asthenosphere⁵³ and thermal boundary conditions fixed at 0 °C at the surface and 1327 °C at the lower boundary, with nil horizontal heat flux across the vertical boundaries³⁵. Temperature is set to 1327 °C in the mantle melting zone. The bulk composition of the mantle melting zone in the model is ultramafic, but enrichment by 25% mafic melt is prescribed in the magmatic channel^{35,48}. $\eta_{ductile}$ (equation 3) of partially molten rocks (with $\xi > 0.1$, equation 10.3) is assigned a low constant value of 10¹⁶ Pa s (Refs. 6,33). A $\eta_{ductile}$ upper limit is set to 10²⁵ Pa s (Refs. 11,35,53). The topographic wedge measures 2.5 km in simulations with central topography, and 1.5 km in simulations with lateral topography, consistent with the change in mean altitude between zones 1-2 and zone 3 (ref. 18).

Additional References

48. Burg, J. P. *et al.* Translithospheric mantle diapirism: Geological evidence and numerical modelling of the Kondyor zoned ultramafic complex (Russian Far-East). *J. Petrol.* **50**, 289–321 (2009).
49. Gerya, T. V. & Yuen, D. A. Robust characteristics method for modelling multiphase visco-elasto-plastic thermo-mechanical problems. *Phys. Earth Planet. Inter.* **163**, 83–105 (2007).
50. Ranalli, G. *Rheology of Earth*. (Springer Sciences and Business Media, 1995).

51. Hirschmann, M. M. Mantle solidus: Experimental constraints and the effects of peridotite composition. *Geochemistry, Geophys. Geosystems* **1**, (2000).
52. Johannes, W. The significance of experimental studies for the formation of migmatites. in *Migmatites* (ed. Ashworth, J. R.) (Blackie & Son Ltd, USA Chapman & Hall, 1985).
53. Turcotte, D. L. & Schubert, G. *Geodynamics*. (Cambridge University Press, 2002).

Supplementary Files

This is a list of supplementary files associated with this preprint. Click to download.

- [SupplementaryDataNatGeoSVZ.docx](#)